May 5, 2009 | vol. 106 | no. 18 | 7265–7680

PNAS

Proceedings of the National Academy of Sciences of the United States of America www.pnas.org

In This Issue

7273 How genes evolve
7281 Predicting reward and punishment
7299 Evidence for superconducting nanotubes
7314 Seaweed employs distributed antifungal defense
7361 Early Egyptian wine made into herbal remedy
7507 Upstream open reading frames have wide impact on protein expression

EVOLUTION

How genes evolve

Many new genes evolve through gene duplication followed by rapid evolution. The rate of the evolutionary process was thought to depend on the interrelationships between a protein's structure and function, and its biological role. Yuri Wolf et al. used a mathematical model to predict the variables that determine the evolutionary rates of change in genes from *Drosophila*, *Aspergillus*, and humans. The authors found that the distribution of evolutionary rates was universal, although their model predicted substantial differences between genes of different age classes. Younger genes—genes whose homologues had a shorter phylogenetic depth—differed significantly on variables correlated to the rate of gene loss, compared to older genes. The older genes are longer and more highly expressed, have a higher intron density, tend to evolve more slowly, and are subject to stronger purifying selection than younger genes. However, the authors identified an overlap between the distributions of these variables for the young and old genes; slow-evolving genes are often lost, whereas fast-evolving genes are sometimes retained for long evolutionary spans. Genetic evolution likely occurs at a relatively stable rate of gene gain and loss, without dominant bursts of genomic innovation, according to the authors. — C.A.

"The universal distribution of evolutionary rates of genes and distinct characteristics of eukaryotic genes of different apparent ages" by Yuri I. Wolf, Pavel S. Novichkov, Georgy P. Karev, Eugene V. Koonin, and David J. Lipman (see pages 7273–7280)

NEUROSCIENCE

Predicting reward and punishment

Neurons releasing dopamine can fire in bursts of activity, the phasic mode, or in a steady pattern, the tonic mode. Previous studies have suggested that the phasic mode facilitates memory acquisition by stamping-in the association with a reward or punishment. Correlating the contribution of each mode of neurotransmitter activity to learning has been difficult because of researchers' inability to turn off one mode of firing. Larry Zweifel et al. developed a technique that inhibits the phasic release of dopamine in mice—without altering the steady release mode—by genetically inactivating the receptor necessary for generating bursts of activity. The altered mice were unaffected in a number of dopamine-related activities, such as motor coordination and working memory, but showed severe learning impairment in cue-dependent tasks such as finding food rewards or predicting an unpleasant event. The authors suggest that bursts of dopamine facilitate learning and the ability to predict positive and negative outcomes, stamping-in the association with reward or punishment. — T.H.D.

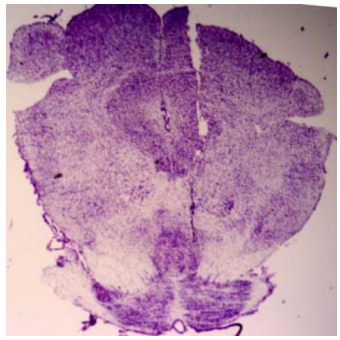

Midbrain section shows tetrode placement into the VTA.

"Disruption of NMDAR-dependent burst firing by dopamine neurons provides selective assessment of phasic dopamine-dependent behavior" by Larry S. Zweifel, Jones G. Parker, Collin J. Lobb, Aundrea Rainwater, Valerie Z. Wall, Jonathan P. Fadok, Martin Darvas, Min J. Kim, Sheri J. Y. Mizumori, Carlos A. Paladini, Paul E. M. Phillips, and Richard D. Palmiter (see pages 7281–7288)

APPLIED PHYSICAL SCIENCES

Evidence for superconducting nanotubes

Fluctuations in electron density are a barrier to superconductivity in one dimension. Superconductivity in carbon nanotubes, which are quasi-one-dimensional, is, therefore, a controversial topic. Researchers have suggested that electron-phonon coupling, which enables the formation of superconducting electron pairs, is increased in nanotubes at smaller diameters, but the problem with fluctuations remains. Regular parallel arrays of nanotubes constitute a possible route to superconductivity, because electron coherence could extend across nanotubes

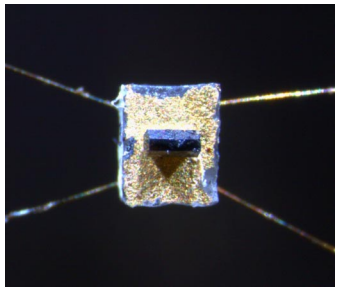

Composite zeolite mounted on a microcalorimeter.

and suppress fluctuations. Rolf Lortz et al. present results from an array of nanotubes fabricated inside a zeolite matrix. The authors observed a characteristic superconducting transition at 15 K in the specific heat of the nanotubes. The contribution of the nanotubes was dwarfed by that of the matrix, but could be extracted by subtracting the signal obtained in a high magnetic field that suppresses superconductivity. The authors compared their results to theory and found that the nanocomposite behaves as a type-II BCS superconductor. — K.M.

"Superconducting characteristics of 4-Å carbon nanotube–zeolite composite" by Rolf Lortz, Qiucen Zhang, Wu Shi, Jiang Ting Ye, Chunyin Qiu, Zhe Wang, Hongtao He, Ping Sheng, Tiezheng Qian, Zikang Tang, Ning Wang, Xixiang Zhang, Jiannong Wang, and Che Ting Chan (see pages 7299–7303)

CHEMISTRY, ECOLOGY

Seaweed employs distributed antifungal defense

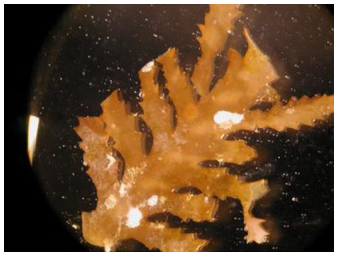

Callophycus serratus sample.

Recently developed analytical techniques have enabled researchers to learn how simple lifeforms, such as algae, control their surface chemistry to protect themselves from microbial pathogens. Amy Lane et al. report that desorption electrospray ionization mass spectrometry (DESI-MS) is a useful tool in this effort. In DESI-MS, a charged spray of organic solvent desorbs molecules from the surface of a sample under ambient atmosphere; the molecules are then ionized and delivered to a mass spectrometer. This technique allowed the authors to explore the surface chemistry of the Fijian seaweed *Callophycus serratus* while leaving the organism intact. Previously, the authors had determined that one subpopulation of *C. serratus* produced a family of diterpene macrolides called bromophycolides, whereas another subpopulation produced a related series of compounds—callophycoic acids and callophycols—that do not possess the macrolide ring structure of the bromophycolides. The authors determined that all of these compounds inhibited growth of a fungal pathogen that affects marine plants. Lane et al. used microscopic inspection, combined with DESI-MS, to show that bromophycolides appeared only within algal tissues and on white patches that covered ≈5% of the algal surface. The patchy surface distribution may indicate a response to wounding, according to the authors. — K.M.

"Desorption electrospray ionization mass spectrometry reveals surface-mediated antifungal chemical defense of a tropical seaweed" by Amy L. Lane, Leonard Nyadong, Asiri S. Galhena, Tonya L. Shearer, E. Paige Stout, R. Mitchell Parry, Mark Kwasnik, May D. Wang, Mark E. Hay, Facundo M. Fernandez, and Julia Kubanek (see pages 7314–7319)

ANTHROPOLOGY

Early Egyptian wine made into herbal remedy

Without the benefits of modern medicine, our human ancestors empirically discovered and exploited natural compounds found in plants as a way to cure their ailments. Patrick McGovern et al. report that ancient Egyptians dissolved herbs, including balm, coriander, mint, and sage, as well as tree resins, into grape wine. The authors present chemical evidence from residues inside an amphora from the tomb of pharaoh Scorpion I of Egypt, dated to 3150 B.C. A later Egyptian amphora, dating from the 4th to 6th centuries A.D. from Gebel Adda in southern Egypt, also tested positive for wine with rosemary and pine resin. The authors used liquid chromatography tandem mass spectrometry to confirm the presence of tartaric acid, the marker compound for grape in the Middle East, and used solid phase microextraction to identify herbal constituents. The research represents an ongoing effort to "reexcavate" ancient medicinal remedies that were lost throughout millennia of human history and might be applied in 21st century health and medicine, according to the authors. — K.M.

Egyptian wine amphora from early Byzantine era. Photo courtesy of W. Pratt, Royal Ontario Museum.

"Ancient Egyptian herbal wines" by Patrick E. McGovern, Armen Mirzoian, and Gretchen R. Hall (see pages 7361–7366)

GENETICS

Upstream open reading frames have wide impact on protein expression

Posttranscriptional regulation of gene expression frequently occurs in the 5′-untranslated region (UTR) of mRNA. Upstream open reading frames (uORFs), located in the 5′-UTR and present in approximately half of human and mouse transcripts, are thought to alter protein expression by disrupting ribosomal movement and efficient translation. Sarah Calvo et al. examined the effects of uORFs by comparing 11,649 matched measurements of mRNA sequence and protein levels from 4 previously published studies, and found a significantly reduced protein-to-mRNA ratio in those genes containing a uORF. The authors quantified the effect size by cloning the 5′-UTR of 25 uORF-containing genes and creating a dual-luciferase reporter and found that the presence of a uORF caused, on average, a 58% decrease in protein levels. The authors found that hundreds of human genes contain uORF polymorphisms and that these polymorphisms influence protein expression. They identified a link between uORF mutations and 11 human diseases, including 3 connections not found in previous research. The authors say these data suggest that uORFs may influence phenotype by decreasing protein levels in thousands of mammalian genes. — C.A.

"Upstream open reading frames cause widespread reduction of protein expression and are polymorphic among humans" by Sarah E. Calvo, David J. Pagliarini, and Vamsi K. Mootha (see pages 7507–7512)

Superconducting characteristics of 4-Å carbon nanotube–zeolite composite

Rolf Lortz[a,b,1], Qiucen Zhang[a,1], Wu Shi[a], Jiang Ting Ye[a], Chunyin Qiu[c], Zhe Wang[a], Hongtao He[a], Ping Sheng[a,2], Tiezheng Qian[c], Zikang Tang[a], Ning Wang[a], Xixiang Zhang[a,3], Jiannong Wang[a], and Che Ting Chan[a]

[a]Department of Physics and William Mong Institute of Nano Science and Technology, and [c]Department of Mathematics, Hong Kong University of Science and Technology, Clear Water Bay, Kowloon, Hong Kong, China; [b]Département de Physique de la Matière Condensée, Université de Genève, Quai Ernest-Ansermet 24, 1211 Genève 4, Switzerland

Communicated by Moses H. Chan, Pennsylvania State University, University Park, PA, December 23, 2008 (received for review September 28, 2008)

We have fabricated nanocomposites consisting of 4-Å carbon nanotubes embedded in the 0.7-nm pores of aluminophosphate-five (AFI) zeolite that display a superconducting specific heat transition at 15 K. MicroRaman spectra of the samples show strong and spatially uniform radial breathing mode (RBM) signals at 510 cm^{-1} and 550 cm^{-1}, characteristic of the (4, 2) and (5, 0) nanotubes, respectively. The specific heat transition is suppressed at >2 T, with a temperature dependence characteristic of finite-size effects. Comparison with theory shows the behavior to be consistent with that of a type II BCS superconductor, characterized by a coherence length of 14 ± 2 nm and a magnetic penetration length of 1.5 ± 0.7 μm. Four probe and differential resistance measurements have also indicated a superconducting transition initiating at 15 K, but the magnetoresistance data indicate the superconducting network to be inhomogeneous, with a component being susceptible to magnetic fields below 3 T and other parts capable of withstanding a magnetic field of 5 T or beyond.

resistance transition | specific heat | superconductivity

Superconductivity in carbon nanotubes (CNTs) is a topic of intriguing interest (1–11). While the small-diameter nanotubes are predicted to have enhanced electron-phonon coupling (3)—a key element responsible for nanotube superconductivity–the associated increase in fluctuation effects is unfavorable to the manifestation of a superconducting transition. The possibility of a Peierls transition in thin nanotubes is a further deterrent to superconductivity (12–17). It follows that the existence of coupling between the nanotubes is important to the realization of its superconducting behavior, since the transverse coherence can suppress fluctuations and lower the Peierls transition temperature, thereby making the appearance of a superconducting transition possible. Owing to its ordered and closely-spaced pore structure (with a 13.6-Å center-to-center separation between the 0.7-nm diameter pores), the AFI zeolite (composition: $Al_{12}P_{12}O_{48}$) with embedded 4-Å carbon nanotubes constitutes an ideal material for the observation of nanotube superconductivity. Indeed, the Meissner effect, a superconducting gap variation as a function of temperature, and the fluctuation supercurrent were observed in these nanocomposites (1), with a transition temperature of 15 K. However, the superconducting resistive transition was not observed.

By increasing the carbon nanotube content with enhanced sample uniformity, we report the carbon nanotube superconducting specific heat transition at 15 K. The specific heat transition is fully suppressed at >2 T. Theory-experiment comparisons show consistent behavior for an inhomogeneous type II superconductor with ≈80 nm clusters of nanotubes weakly linked to form a bulk superconducting composite. Four-terminal resistive data and differential resistivity measurements both show a clear superconducting transition at 15K, but they also point to the existence of a phase incoherent fluctuating superconducting condensate in nanotubes at 5 T or above.

Results

Samples. AFI zeolite crystals (≈100 μm in diameter and 500 μm long) containing the tripropylamine (TPA) precursor were first heated at 580 °C in 0.7 atm of nitrogen and 0.3 atm of oxygen for 8 h to *remove* the TPA, and then in 0.7 atm nitrogen and 0.3 atm of ethylene at the same temperature for 8 h. This method of heating is noted to differ from the earlier approach in which the nanotubes were obtained from direct conversion of TPA through heating the crystals in vacuum (18–20). In the present approach, the nanotubes were converted from ethylene instead of the original TPA. As such, the possibility of unintentional nitrogen doping (as TPA contains nitrogen) is minimized. The heated crystals were characterized by Raman spectra (with laser wavelength of 514.5 nm), as shown in Fig. 1. Two peaks, one at 510 cm^{-1} and one at 550 cm^{-1}, are noted by arrows. They respectively correspond with the (4, 2) and (5, 0) carbon nanotubes' radial breathing modes (RBM) as determined by resonant Raman measurements and first-principles calculations (21). The magnitude of the RBM, relative to the G-band carbon-carbon Raman signal at 1,600 cm^{-1}, is significant as it provides evidence (apart from the ratio of coupling strengths) of the percentage of the carbon in nanotube form. We have done a statistical comparison of the 2 methods of heating. In the inset of Fig. 1, the proportion of the 550 cm^{-1} peak (delineated by green bars) is seen to be ≈10% of the G-band signal after subtracting the background, significantly higher than the ≈5% average RBM signals observed in the vacuum heat-treated samples (delineated by red bars). The superconductivity is attributed to the (5, 0) carbon nanotubes.

The sample for the specific heat was prepared by aligning the heated AFI crystals along their *c*-axis and using GE7031 varnish to glue them together into a 3 × 3 × 0.5 mm platelet, with a total weight of 7.9 mg, in which 5.2 mg was the weight of the crystals. The measurements were carried out by using the standard AC technique (22) where the sample was attached to a suspended sapphire chip with deposited resistive Joule heater. An AuFe/Chromel thermocouple was attached to the chip to measure the temperature modulation of the chip relative to a thermal reservoir. The field dependence of the thermocouple's sensitivity was calibrated very precisely in a subsequent experiment using an Ag calibration sample. To achieve sufficient relative resolution in the measurement of the AC voltage from the thermocouple, a picovolt amplifier, which is free of 1/*f* noise, in combination with a digital lock-in amplifier was used, and the

Author contributions: P.S. designed research; R.L., Q.Z., W.S., J.T.Y., Z.W., H.H., Z.T., N.W., X.Z., and J.W. performed research; R.L., Q.Z., C.Q., P.S., T.Q., and C.T.C. analyzed data; and R.L., Q.Z., and P.S. wrote the paper.

The authors declare no conflict of interest.

[1]R.L. and Q.Z contributed equally to this work.

[2]To whom correspondence should be addressed. E-mail: sheng@ust.hk.

[3]Present address: Research and Development, King Abdullah University of Science and Technology, Thuwal, Saudi Arabia.

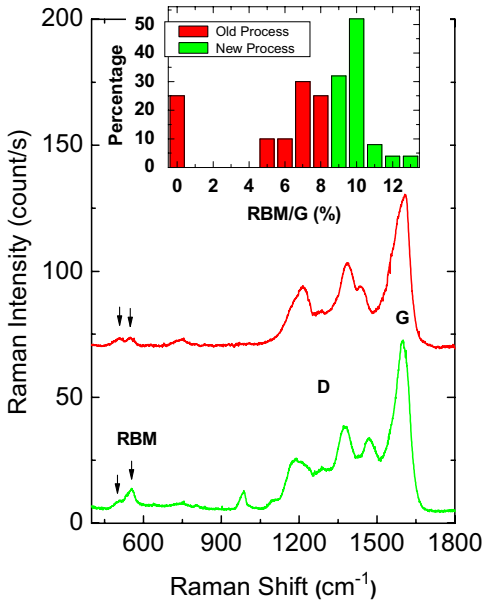

Fig. 1. Comparison of the Raman spectra for the old (delineated by the red curve) and the current (delineated by the green curve) heating processes. The Raman excitation wavelength is 514.5 nm. The RBM ratio to the G band is nearly doubled for the current process. For clarity, the 2 spectra are vertically displaced from each other. Inset: Proportion of the samples exhibiting the various RBM ratio to the G band.

measurements were performed during slow temperature sweeps of 0.02 K/min at a time constant of 10 s and a modulation frequency of ≈1.5 Hz. The AC measurements were combined with a "long" relaxation technique to achieve an accuracy of the total heat capacity determination of <1%. The contribution of the 2.7 mg of dried varnish was corrected using literature data (23). Measurements were performed in magnetic fields of 0, 0.4, 1, 2, and 5 T, applied both parallel and perpendicular to the *c*-axis.

Specific Heat Experiments on CNT@AFI. The total specific heat* of the sample *C*/*T*, corrected for the GE varnish contribution, is shown in the inset of Fig. 2*A*. The tiny superconducting transition signal becomes visible only after subtracting the phonon contribution which is dominated by the AFI host, under an applied field of 5 T. We used the data taken at 5 T for this purpose as earlier magnetization measurements (1) suggest that the upper critical field is below 5 T. The resulting $C^{\text{electr}}(H)/T$ data are plotted in Fig. 2*A* (perpendicular) and 2*B* (parallel). On a scale that is ≈3 orders of magnitude smaller than the total specific heat, a broad anomaly was visible in zero field with maximum at 12 K and onset at ≈15 K. A magnetic field further broadened the anomaly and shifted it down to lower temperatures. At the lowest temperatures, an exponential increase of the specific heat was observed in zero field which suggests a standard s-wave order parameter. Surprisingly, there was only a very small amount of magnetic anisotropy, a point to be discussed later. We used the criterion that C^{electr}/T approaches zero at $T = 0$ for a fully gapped superconductor to estimate the Sommerfeld constant $\gamma_n = 2.2 \pm$

*The total *C*/*T* measured at 15 K is 5.5× 10^{-6} J/K^2 (corrected for GE varnish), and C^{electr}/T = 1.5× 10^{-8} J/K^2 represents the low temperature difference between the 5-T data and the zero field data. This value was taken to be γ_n. The numbers in the text were obtained from the following useful data. AFI zeolite density is 1.87 g/cm^3 and the (5,0) carbon nanotube's unit cell length is 4.32 Å, with 20 carbon atoms to each unit cell. Per unit length of the pore [filled with (5,0) carbon nanotubes], the mass of the carbon is 32% that of AFI zeolite, which has the composition of $Al_{12}P_{12}O_{48}$, with a unit cell length of 8.4 Å. In Fig. 2, the mass used in the C^{electr}/T normalization was mostly that of AFI zeolite.

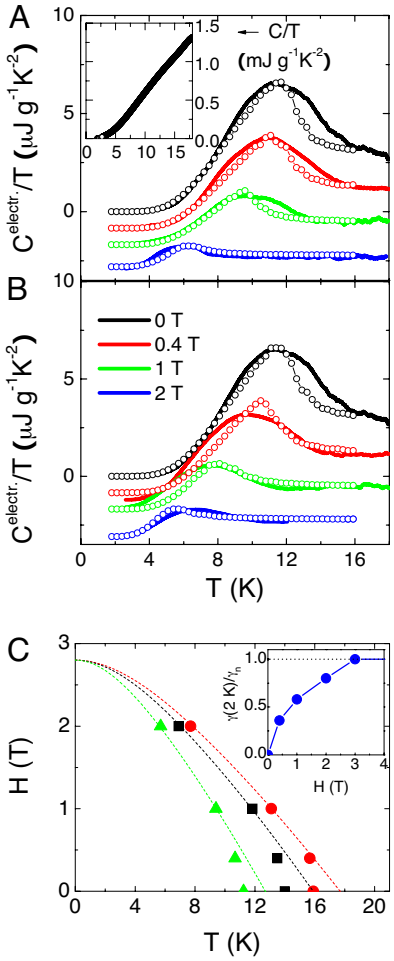

Fig. 2. Specific heat data of the CNT@AFI sample. Electronic contribution $C^{electr.}/T$ of superconducting nanotubes encaged in the pores of AFI single crystals for magnetic fields applied perpendicular (*A*) and parallel (*B*) to the nanotubes. Solid lines represent the data; open circles are theoretical fits with T_c = 15 K and parameter values given in the text. For clarity, the 0.4, 1, and 2 T curves have been shifted downwards by 1.7, 3.4, and 5.1 μJ/g/K^2, respectively. The data are normalized by the mass of the sample as the total amount of nanotubes in this composite material is unknown (20). Data's error bar is about ± 0.5 μJ/g/K^2. Inset of (*A*): Zero field total specific heat of the AFI single crystals with encaged nanotubes in the pores. The Sommerfeld constant of the superconducting contribution is 370 times smaller than the total specific heat at 15 K. (*C*) Magnetic phase diagram derived from the specific heat (field applied perpendicular to the nanotubes). Because of the fluctuation-induced broadening of the transition, 3 different criteria have been used to trace $T_c(H)$: The upper onset of the transition (red dots), the midpoint of the broadened specific-heat jump (black squares), and the specific-heat maximum (green triangles). The dashed lines are extrapolations toward H_{c2} (0) according to a fit with the standard WHH model. Inset: Plot of the normalized low-temperature electronic specific heat at 2 K as a function of the magnetic field.

0.4 mJ/mole of (5, 0) unit cells/K^2 for the superconducting fraction of the sample*. This value is 370 times smaller than the total specific heat of the AFI crystals at 15 K, and we have used for normalization the number of nanotube unit cells in the total length of the AFI pores in the sample, assuming 100% occupancy. This is certainly not true, but the value allowed us to compare with the BCS prediction, $\gamma_n = (2/3)\pi^2 k_B^2 N(0)$, where k_B is Boltzmann's constant, for an estimate of the true filling factor of the pores. Recent calculations (21) suggest a density of states at the Fermi level $N(0)$ = 5/eV/unit cell, implying a theoretical value of γ_n = 23.4 mJ/mole of (5, 0) unit cells/K^2. This comparison allows us to conclude that 10 ± 2% of the total

length of the pores of the AFI crystals were filled with superconducting material. Fig. 2*C* shows a magnetic phase diagram derived from the specific-heat data in field applied perpendicular to the CNTs. As the transition is broadened by fluctuations, we used three different criteria to trace the upper critical field line, that is, the upper onset of the superconducting transition (highest temperature where the data starts to deviate from γ_n), the midpoint of the broadened specific-heat jump, and the maximum of the specific-heat anomaly. We used the standard model of Werthamer, Helfand, and Hohenberg (WHH model; 24) to extrapolate the upper critical field to H_{c2} (0). The 3 curves converge to H_{c2} (0) = 2.8 ± 0.4 T. Indeed, at 3 T no more signature of superconductivity was observed in the experiments. The deviation of the data from the model close to $T_c(H)$ is almost certainly related to the presence of strong phase fluctuations, which lower the transition temperature somewhat from the BCS value and broaden the transition. The inset to Fig. 2*C* shows the normalized magnetic field dependence of the electronic specific heat at 2 K, which also indicates H_{c2} (0) ≈3 T. Note that the concave behavior of this quantity is unlikely to be related to the presence of nodes in the order parameter. A linear dependence of the low temperature specific heat for s-wave superconductors is only expected at magnetic fields much smaller than H_{c2}.

Theoretical Modeling of the Specific Heat Data. The peaks are much broader than those observed in bulk superconductors, and there is no significant anisotropy in the data. We attribute both features to the finite size of the superconducting nanotube clusters. To substantiate this attribution and to extract the parameter values relevant to the sample, we used the Bardeen-Cooper-Schrieffer (BCS) specific heat expression (25), with the gap function $\Delta(T,H)$ simulated by an anisotropic Ginzburg-Landau (GL) model for finite-sized superconducting clusters (2). Here,

$$C^{electr} = 2\beta^2 k_B \int g(\varepsilon)\exp(\beta E)[1 + \exp(\beta E)]^{-2} \cdot \left(E^2 + \frac{1}{2}\,\beta\,\frac{d\Delta^2}{d\beta} \right) d\varepsilon$$

where $\beta = 1/k_BT$, $E = [\varepsilon^2 + \Delta^2]^{1/2}$, $g(\varepsilon) = N(0)\sqrt{1 + \varepsilon/\varepsilon_F}$, and ε_F is the Fermi energy. By setting $[\Delta/\Delta(0)] = \sqrt{\langle|\psi|^2/|\psi_0|^2\rangle}$, we evaluate the normalized gap function through the ensemble-averaged (denoted by the angular brackets) values of the absolute-value square of the complex GL order parameter ψ. Here, the subscript 0 denotes the value at H, $T = 0$, and $\Delta(0) = gk_BT_c$ with the value of g to be fixed by the low temperature data.

The values of g = 3 ± 0.2 and T_c = 15 ± 1 *K* can be easily obtained from Monte Carlo simulations (2, 26) on zero-field $\langle|\psi^2|/|\psi_0|^2\rangle$ for a sample of size 6 × 6 × 3 (in units of the zero-temperature coherence length ξ_0, with 3 being along the *c*-axis direction), with good fits obtained to both the experimental peak height and the observed low temperature behavior as shown by the connected symbols in Figs. 2*A* and 2*B*. Here, the theoretical values are normalized to the experimental value of γ_n. It is noted that $\Delta(0) = 3k_BT_c$ is larger than the BCS value of $\Delta(0) = 1.76k_BT_c$, but the temperature dependence of the normalized gap is in very good agreement with that obtained earlier via different means (1). For finite magnetic fields, we also obtained very good fits to the data in both orientations without further changes in the parameter values, with dimensionless $\bar{B}$ = 0.04, 0.1, and 0.2 to correspond with 0.4, 1, and 2 T, respectively. Since $\bar{B} = B\xi_0^2/\Phi_0$ with $\Phi_0 = hc/2e$ being the quantum flux, the good agreement between theory and experiment implies ξ_0 = 14 ± 2 nm. As the scaled problem is isotropic in terms of the interactions, ξ_0 is the only coherence length obtainable. The slight difference between the 2 orientations at intermediate fields is due to the shape of the finite-sized sample. We have also used the low temperature asymptotes as an indicator for the fraction $f_n(H)$ of the sample turned to normal by the magnetic field, so that the plotted theory curves represent $f_n + (1 - f_n)C_{es}/(\gamma_n T)$. No useful anisotropy information may be obtained from the data, owing to the lack of information on either the actual physical geometry of the nanotube clusters, or the ratio in the coherence lengths along the 2 principal directions†. From our data fitting, an estimate of zero-temperature $H_c \cong 100 \pm 50$ G and an effective magnetic penetration length $\lambda \cong 1.5 \pm 0.7$ μm were obtained. The values of λ and ξ_0 were noted to be remarkably consistent with those estimated earlier (2).

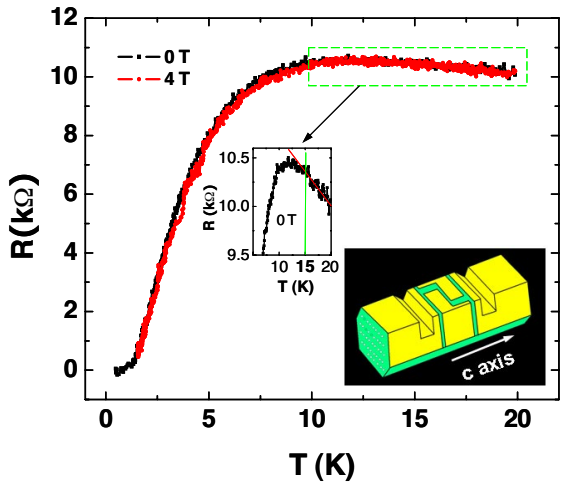

Fig. 3. Resistance plotted as a function of temperature for the 4-terminal sample, measured at 10 nA. The geometry of the sample is illustrated in the cartoon inset, with yellow indicating gold coating and green the AFI crystal surface. The slice between the 2 grooves is 5 μm thick. The enlarged section shows the transition starts at 15 K. Up to 4 T, there is no appreciable change in the $R(T)$ behavior.

Electronic Transport Characteristics of CNT@AFI. As the specific heat was measured with reference to the 5 T values, any superconducting order not quenched at 5 T would not be fully manifested in the data. Transport measurements, however, may yield some information regarding the existence of (fluctuating) superconducting condensate in individual nanotubes beyond 5 T.

To measure the electric transport characteristics, we prepared the sample by selecting an AFI zeolite crystallite (50 × 50 × 300 μm) and using the Focused Ion Beam (FIB, Seiko SMI2050) to delineate a 5-μm slice (see the cartoon inset of Fig. 3) containing nanotubes perpendicular to the slice. To provide electrical contact, 50 nm of Ti and 150 nm of Au were sputtered on the surface of AFI as well as the fresh ends of the single-walled nanotubes (SWNTs). FIB was again used to define the 4-terminal electrode configuration on the AFI surface as shown by the cartoon inset in Fig. 3. The 2 voltage leads in the center were separated by 100 nm. Further annealing in vacuum (10^{-6} Torr) at 500–600 °C reduced the contact resistance between SWNTs and Au/Ti. It should be noted that owing to the fact that the nanotubes were situated only ≈10 Å below the AFI surface,

†For example, if it is known that the average physical size of the nanotube clusters is 5 times as long (along the *c*-axis) as it is wide (i.e., 80 nm wide and 400 nm in length), then from our simulation results it can be concluded that the coherence length in the *z* direction is 10 × ξ_0, which implies a factor of 100 in the ratio of the coupling strength along the transverse and longitudinal directions.

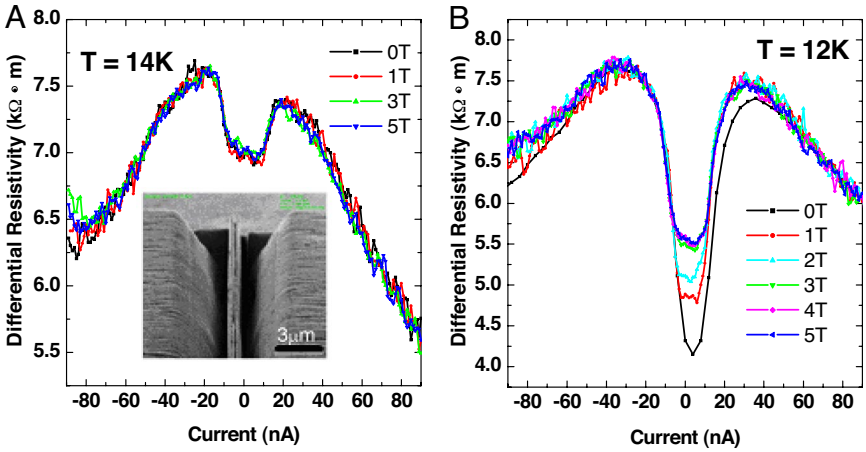

Fig. 4. Magnetic field dependence of the differential resistivity for the 2-terminal sample. (*A*) At 14 K, the application of a magnetic field of up to 5 T had no effect on the differential resistivity dip at small bias current. (*B*) At 12 K, there is clear positive magnetoresistance up to 3 T. A scanning electron microscopy image of the sample is shown in the inset.

sample contact with the electrodes was good, in particular as the AFI surface is imperfect.

Low temperature measurements of resistance vs. temperature were made with a series resistance of less than 15 Ohms. As the AFI zeolite is insulating, the conductance of the sample directly reflects the conductance of the SWNTs.

Fig. 3 shows the resistance measured in the 4-terminal configuration plotted as a function of temperature. It is seen that the transition initiates at 15 K (see the inset showing the enlarged section), with resistance decreasing smoothly toward zero. The resistance vs. temperature behavior was not changed under a 4-T magnetic field (applied perpendicular to the *c*-axis of the AFI crystal), suggesting the superconducting component, in this case, may consist of thin bundles of coupled nanotubes. Clearly, such a component would not be detectable by specific heat measurements with a quenching field of 4–5 T.

In another sample prepared for 2-terminal measurement (in which the central slice is only 1 μm wide), differential resistivity of the SWNTs array was measured as a function of the bias current.[‡] At 16 K, there was a broad resistivity peak around low current bias, presumably due to electron-electron interaction effects in SWNTs (27). A sudden change occurred at T_c = 15 K with the onset of a dip around the low current bias. In Fig. 4, we show the measured resistivity dip at 14 K (Fig. 4*A*) and 12K (Fig. 4*B*). It is seen that as temperature decreased, the depth of the measured resistivity dip increased. At 14 K, there was no magnetoresistance up to 5 T (Fig. 4*A*), but at 12 K, there was positive magnetoresistance up to 3 T (noted to be consistent with the specific heat data), but beyond which the dip did not change as the field was increased to 5 T (Fig. 4*B*). The dip disappeared as the temperature was raised to 15 K. These characteristics strongly suggest the superconducting component of the sample to be inhomogeneous, with part of the network susceptible to magnetic effects below 3 T (the part where the nanotubes are coupled through Josephson interaction, with condensation starting at below 14 K) and which can be in series with the other parts (thin bundles or even single nanotubes) capable of withstanding a much higher magnetic field, maybe up to the Pauli limit, whereby the singlet spin pairing is broken, estimated to be 30–40 T. While the Josephson coupled array is detectable by the specific heat, the thin bundle component of the network is only measurable through the transport measurements. Owing to the large sample resistance (on the order of 7 mega Ohms), the *R* vs. *T* transition behavior was not seen in the sample with the 2-terminal configuration.

Conclusions

In conjunction with the previous Meissner effect data (1), the specific heat and differential resistivity measurements show that nanostructure in the form of thin tubes can induce superconductivity in undoped carbon, which was not previously known to be superconducting. Such superconductivity with 1-D elements displays a qualitatively BCS-type behavior on the scale of 10 nm or more. However, its intrinsic characteristics at the level of individual nanotubes still remain to be further explored[§].

[‡]Differential resistance measurement was done by using a negative, 2-nA and 0.02-s current pulse followed by a similar positive pulse, and measuring the voltage difference. This is repeated for every current value.

[§]We note that in spite of the different samples and their fabrication processes, there is consistency in the measured transition temperature. This could be due to the ordered AFI crystal structure. Also, it should be noted that the constancy of the 15 K transition temperature greatly decreases the possibility that the superconductivity is due to unintentional nitrogen doping, since in the current sample fabrication approach the nanotubes are formed from ethylene (instead of TPA as in the original approach), which has no nitrogen. If the superconductivity was due to nitrogen doping, then at least the transition temperature should be sensitive to the doping level. The different fabrication approaches should, at a minimum, alter the nitrogen doping level. Thus, the constancy of the transition temperature may be regarded as strong evidence against nitrogen doping as the cause of the observed superconductivity. The lack of magnetic anisotropy also represents a significant difference with the previous samples. This could be due to the larger transverse dimension of the nanotube clusters in the present samples.

ACKNOWLEDGMENTS. We thank Bei Zhang, Ling Li, Z. M. Li, Fuyi Jiang, Wei Min Chung, and Milky Tang for technical support and Paul Chu for making it possible to obtain the essential pieces of equipment used in the experiments. P.S. thanks the late Leroy Chang for his continued encouragement. R.L. thanks Dirk van der Marel and Jean-Marc Triscone for their support during the experiments in Geneva. This work was supported by the Research Grants Council of Hong Kong Grants CA04/04.SC02, DSC104/05.SC01, and VPAAO04/05.SC01.

1. Tang ZK, et al. (2001) Superconductivity in 4-Angstrom single-walled carbon nanotubes. *Science* 292:2462–2465.
2. Qiu C, Qian T, Sheng P (2007) Meissner effect in a system of coupled one-dimensional superconducting wires: Monte Carlo simulations. *Phys Rev B* 75:024504.
3. Benedict LX, Crespi VH, Louie SG, Cohen ML (1995) Static conductivity and superconductivity of carbon nanotubes: Relations between tubes and sheets. *Phys Rev B* 52:14935–14940.
4. Kasumov A, et al. (2003) Quantum transport through carbon nanotubes: Proximity-induced and intrinsic superconductivity. *Phys Rev B* 68:214521.

5. Kociak M, et al. (2001) Superconductivity in ropes of single-walled carbon nanotubes. *Phys Rev Lett* 86:2416–2419.
6. Takesue I, et al. (2007) Superconductivity in entirely end-bonded multi-walled carbon nanotubes. *Physica C* 460-462:111–115.
7. Takesue I, et al. (2006) Superconductivity in entirely end-bonded multiwalled carbon nanotubes. *Phys Rev Lett* 96:057001.
8. Sasaki K-I, Jiang J, Saito R, Onari S, Tanaka Y (2007) Theory of superconductivity of carbon nanotubes and graphene. *J Phys Soc Jpn* 76:033702.
9. Morpurgo AF, Kong J, Marcus CM, Dai H (1999) Gate-controlled superconducting proximity effect in carbon nanotubes. *Science* 286:263–265.
10. Tsuneta T, Lechner L, Hakonen PJ (2007) Gate-controlled superconductivity in a diffusive multiwalled carbon nanotube. *Phys Rev Lett* 98:087002.
11. Barnett R, Demler E, Kaxiras E (2005) Electron-phonon interaction in ultrasmall-radius carbon nanotubes. *Phys Rev B* 71:035429.
12. Huang Y, Okada M, Tanaka K, Yamabe T (1996) Estimation of Peierls-transition temperature in metallic carbon nanotube. *Sol Stat Comm* 97:303–307.
13. Sédéki A, Caron LG, Bourbonnais C (2000) Electron-phonon coupling and Peierls transition in metallic carbon nanotubes. *Phys Rev B* 62:6975–6978.
14. Bohnen K-P, Heid R, Liu HJ, Chan CT (2004) Lattice dynamics and electron-phonon interaction in (3,3) carbon nanotubes. *Phys Rev Lett* 93:245501.
15. González J, Perfetto E (2005) Coulomb screening and electronic instabilities of small-diameter (5,0) nanotubes. *Phys Rev B* 72:205406.
16. Connétable D, Rignanese G-M, Charlier J–C, Blasé X (2005) Room temperature Peierls distortion in small diameter nanotubes. *Phys Rev Lett* 94:015503.
17. Fernández-Serra MV, Blasé X (2008) Zone-center instability of C(5,0) carbon nanotubes inside AlPO4–5 channels. *Phys Rev B* 77:195115.
18. Wang N, Tang ZK, Li GD, Chen JS (2000) Single-walled 4-Å carbon nanotube arrays. *Nature* 408:50–51.
19. Li ZM, et al. (2001) Polarized absorption spectra of single-walled 4-Å carbon nanotubes aligned in channels of an $AlPO_4$-5 single crystal. *Phys Rev Lett* 87:127401.
20. Li ZM, et al. (2004) Synthesis of 4-Å single-walled carbon nanotubes in catalytic Si-substituted $AlPO_4$-5 molecular sieves. *Appl Phys Lett* 85:1253–1255.
21. Liu HJ, Chan CT (2002) Properties of 4-Å carbon nanotubes from first-principles calculations. *Phys Rev B* 66:115416.
22. Sullivan PF, Seidel G (1968) Steady-state, AC-temperature calorimetry. *Phys Rev* 173:679–685.
23. Heessels JT (1971) Specific heat of General Electric 7031 varnish from 2 to 80 K. *Cryogenics* 11:483–484.
24. Werthamer NR, Helfand E, Hohenberg PC (1966) Temperature and purity dependence of superconducting critical field H_{c2}. III. Electron spin and spin-orbit effects. *Phys Rev* 147:295–302.
25. Tinkham M (1996) *Introduction to Superconductivity*, (McGraw-Hill, New York) 2nd Ed, pp 124.
26. Scalapino DJ, Sears M, Ferrell RA (1972) Statistical mechanics of one-dimensional Ginzburg-Landau fields. *Phys Rev B* 6:3409–3416.
27. Bockrath M, et al. (1999) Luttinger-liquid behaviour in carbon nanotubes. *Nature* 397:598–601.